

Article

# Kelvin-Helmholtz Billows Induced by Shear Instability along the North Passage of the Yangtze River Estuary, China

Jian Shi <sup>1,2</sup> , Chaofeng Tong <sup>1,2</sup>, Jinhai Zheng <sup>1,2,\*</sup>, Chi Zhang <sup>2,\*</sup> and Xiangyu Gao <sup>3</sup>

<sup>1</sup> Key Laboratory of Coastal Disaster and Defence (Hohai University), Ministry of Education, Nanjing 210098, China; jianshi@hhu.edu.cn (J.S.); Chaofengtong@hhu.edu.cn (C.T.)

<sup>2</sup> College of Harbor, Coastal and Offshore Engineering, Hohai University, Nanjing 210098, China

<sup>3</sup> Nanjing Hydraulic Research Institute, Nanjing 210024, China; xygao@nhri.cn

\* Correspondence: jhzheng@hhu.edu.cn (J.Z.); zhangchi@hhu.edu.cn (C.Z.)

Received: 14 February 2019; Accepted: 27 March 2019 ; Published: 2 April 2019



**Abstract:** Kelvin-Helmholtz (K-H) instability plays a significant role in mixing. To investigate the existence of K-H instability along the North Passage of the Yangtze River Estuary, the non-hydrostatic model NHWAVE is utilized to simulate the fresh-salt water mixing process along the North Passage of the Yangtze River Estuary. Using high horizontal resolution, the structure of K-H billows have been successfully captured within the Lower Reach of the North Passage. The K-H instability occurs between the max flood and high-water slack. The duration and length scale of the K-H billows highly depends on the local interaction between fresh-water discharge and tide. The horizontal length scale of the instability is about 60 m, similar to the observations in other estuaries. In the vertical direction, the K-H billows exist within the pycnocline with length scale ranging from 6 to 7 m. The timescale of the billows is approximate 6 min. By analyzing the changes of potential energy during the mixing process, results show that the existence of K-H instability induces intense vertical mixing, which can greatly increase mixing efficiency in the North Passage of the Yangtze River Estuary.

**Keywords:** non-hydrostatic wave model; Kelvin-Helmholtz (K-H) instability; salt-fresh water mixing; Yangtze River Estuary

## 1. Introduction

An estuary is a place where a freshwater river meets the salty open-sea. The hydrodynamics in estuaries are very complex due to the presence of multi-scale physical processes, such as river discharge, tides, winds, waves and offshore currents [1–3]. The periodic mixing and stratification induced by the interaction of river discharge and tidal current plays an important role in mass transport and water quality in estuaries. Tidal-scale processes in fresh-salt water mixing are well understood through in situ observations, laboratory experiments and numerical simulations, however, relative little is know about the hydrodynamic processes on intra-tidal time scales. These small scale flow structures, such as turbulence and instabilities, are the dominant mechanism for the transition from organized flow to turbulence, which is critical to the understanding of the hydrodynamics and mass transport in estuarine areas [4–7].

The Kelvin-Helmholtz (K-H) instability is one of the intra-tidal scale process, which is a common phenomenon of sheared flows in ocean. The theoretical studies of K-H instability originate from Thomson [8] and von Helmholtz [9]. These theories describe the development of the instability and the transition to turbulent mixing in fluids with velocity shear. K-H instability can occur when the destabilizing influence of the velocity shear overcomes the stabilizing effect of the buoyancy force.

Miles [10] and Howard [11] showed that a necessary condition for K-H instability in a parallel, stratified, inviscid flow, is that the gradient Richardson number ( $Ri = N^2/S^2$ , where  $N = \sqrt{-(g/\rho)(\partial\rho/\partial z)}$  is the Brunt-Väisälä frequency,  $S = du/dz$  is the velocity shear,  $g$  is the gravity acceleration,  $\rho$  is density and  $u$  is a representative flow speed) is less than 0.25 somewhere in the flow. However, it has been demonstrated this criterion is not sufficient [12], because it is possible to have a stable shear layer when  $Ri < 0.25$  at the pycnocline. Fringer and Street [13] found the interfacial wave can be stable with  $Ri < 0.25$ , but unstable perturbations occurred when  $Ri < 0.13$ . Barad and Fringer [14] used an adaptive numerical method to evaluate the critical  $Ri$  for instability, and the result showed a similar value of  $Ri < 0.1$  is required for instability. Based on laboratory experiments, Fructus et al. [15] proposed a new criterion for instability, which is  $L_x/\lambda > 0.86$ , where  $L_x$  is the length of the region with  $Ri < 0.25$  and  $\lambda$  is the wave width. Another alternative criterion for instability is based on the linear stability analysis with the Taylor-Goldstein equation. Troy and Koseff [16] used the equation to derive the criterion for instability, which requires  $\bar{\sigma}_i T_w > 5$ , where  $T_w$  is the time the fluid spends in region with  $Ri < 0.25$  and  $\bar{\sigma}_i$  is the averaged growth rate of the instabilities in the region.

In situ observations of K-H instabilities are few due to the limitation of instruments in recording the spatial distribution of density with high resolution. The first observation of K-H instability was conducted by Woods [17]. Through a dye-release experiment in the stratified thermocline of the Mediterranean Sea, the K-H billows associated with internal waves were successfully observed. However, most observations of K-H billows were obtained by echo sounder. Geyer and Smith [18], Geyer and Farmer [19] investigated the existence of K-H billows at the Fraser River Estuary, Canada. The images of K-H billows were most apparent during ebb tide. During the flood tide, there is some mixing but not sufficient to cause instability. Bourgault et al. [20] undertook a field experiment in the St. Lawrence Estuary, but instabilities were detected during both of ebb and flood tide. That means the occurrence of K-H instability depends on the local hydrodynamics and could vary due to the changes of upstream discharge and tides from open-sea. Although the occurrence of K-H instability varies in estuaries, it is consistent that the K-H instability occurs in the pycnocline rather than at the bottom and it is the main mechanism for mixing in the pycnocline [21].

The length scales of K-H billows vary significantly in estuaries. The observation conducted by Geyer and Farmer [19] showed K-H billows with a wavelength of approximate 10 m. In the St. Lawrence estuary, however, the observed length scale is 140–150 m and the vertical size is 10–25 m. Tedford et al. [22] analyzed observations made in the Fraser River Estuary. The length scale of the instabilities is impacted by both of discharge and tidal current. The horizontal length of the billows ranges from 20 to 65 m. More recently, Chang et al. [23] captured a train of K-H billows with a horizontal length scale of 200 m in the Kuroshio off southeastern Taiwan.

Although there is not a consistent length scale of the billows, the observations has indicated that the height to length ratio of K-H billows is about 0.1 [24]. Thus, the typical resolution for well simulating the billows are at least 10–150 m in the horizontal direction and 1–15 m in the vertical direction. Furthermore, high resolution field measurements in the Connecticut River estuary [21,25] have proved the existence of secondary instabilities with wavelength of 0.5–1 m, which play an important role in the turbulent mixing within the pycnocline. That means accurate simulation of the K-H instabilities needs high spatial resolution with grid size of O(0.1 m)–O(1 m). Such small spatial grid is very time consuming in large scale ocean model. Most of the existing ocean models, such as ROMS [26], FVCOM [27] and Delft3D [28,29], are based on the hydrostatic assumption. The vertical accelerating terms are omitted in the momentum equation, hence the vertical mixing process cannot be well represented.

To well capture K-H instability during fresh-salt water mixing in estuaries, non-hydrostatic models are needed, in which the total pressure is divided into two parts: dynamic pressure and hydrostatic pressure. The dynamic pressure can be obtained by solving the pressure Poisson equation. Compared with hydrostatic models, non-hydrostatic models can simulate dispersive waves, strongly stratified fluids and flows over abrupt topography changes, in which the effects of vertical acceleration

are not neglected. The free surface in non-hydrostatic models is assumed to be a single value function of the horizontal coordinate, thus, the surface elevation can be obtained by integrating the continuity equation over depth. Thus, the models are computationally more efficient with the lack of free surface tracking. However, the application of non-hydrostatic model in large-scale simulation is still very time consuming. In coastal and estuarine areas, high resolution non-hydrostatic simulations are limited to domains with lengths of  $O(100\text{ km})$  and most of the simulations are based on two dimensional domain. Özgökmen et al. [30] studied turbulent mixing in the Red Sea Outflow Plume using a non-hydrostatic model. The spatial grid size is 73 m. This two dimensional model revealed the interaction between shear-induced mixing and internal waves, but the horizontal resolution was too coarse to capture the evolution of K-H billows. Wang et al. [31] applied the non-hydrostatic model SUNTANS [32] to resolve small scale intra-tidal dynamics for the Snohomish River Estuary. The results showed that the non-hydrostatic effect is not necessary for simulation of large spatial-temporal scales of estuarine flow, but is very important for small-scale flow structures. Vlasenko et al. [33] simulated the evolution of a river plume using a spatial resolution of 12.5 m. The model can predict the fine internal structures of the plume. It can be seen non-hydrostatic model can well simulate the detailed plume structure in estuary with spatial resolution of  $O(10\text{m})$ . However, finer grid is needed to investigate the structures of the instabilities.

The Yangtze River, with length of 6400 km, is the longest river in Asia. Its annual mean freshwater discharge is  $28,630\text{ m}^3/\text{s}$  according to measurements at Datong gauge station [34]. The Yangtze River estuary (YRE), which is 120 km in length and 90 km in width at the mouth, is characterized by the three-order bifurcations and four outlets (Figure 1). The mass mixing and transport are very complicated due to the interactions of river discharge, tides, waves and wind in the estuary [35–38]. Among the dominant mechanisms leading to mixing, such as bottom stirring, wind stirring and K-H instability, research on K-H instabilities are rare in this area. No observed images or numerical simulations of K-H billows have been published up to now. Pu et al. [39] calculated the gradient Richardson number ( $Ri$ ) along the North Passage. The results showed the values of  $Ri$  is less than 0.25 at the interface within the middle and lower reaches, suggesting the occurrence of K-H instability there. Following the previous discussion the Richardson number is not condition sufficient for the KH instability to occur, thus they did not suggest its existence but rather the possibility that such an instability might occur. To explore whether K-H billows occur along the North Passage of the Yangtze River Estuary, a non-hydrostatic model is used to predict the mixing process in this area. The following parts are organized as: in Section 2, the governing equation, numerical schemes and model setup are briefly discussed. In Section 3, the results are compared with observations. The characteristics of K-H billows are analyzed in Section 4. Finally, concluding remarks are given in Section 5.

## 2. Methodology

### 2.1. Study Area

In 2010, the Deep Navigation Channel (DNC) was constructed within the North Passage of YRE. The northern and southern dikes are about 60 km in length and the width of the DNC is around 400 m with a mean lowest water depth of 12.5 m. The width of the DNC is much smaller than the channel length. Due to the existence of the two dikes, the along channel velocity is much larger than the cross channel one, so flow within the DNC can be approximated as vertical two-dimensional.

In the present investigation, we focus on the vertical salt-fresh water mixing in intra-tidal scales. Observations from fieldwork conducted in April 2009, including sea level, velocities and salinity, provide boundary conditions and validation data for the model. The computational domain covers the North Passage beginning from the gauge station CS0 extending to CS4 close to the North Passage exit (Figure 1).

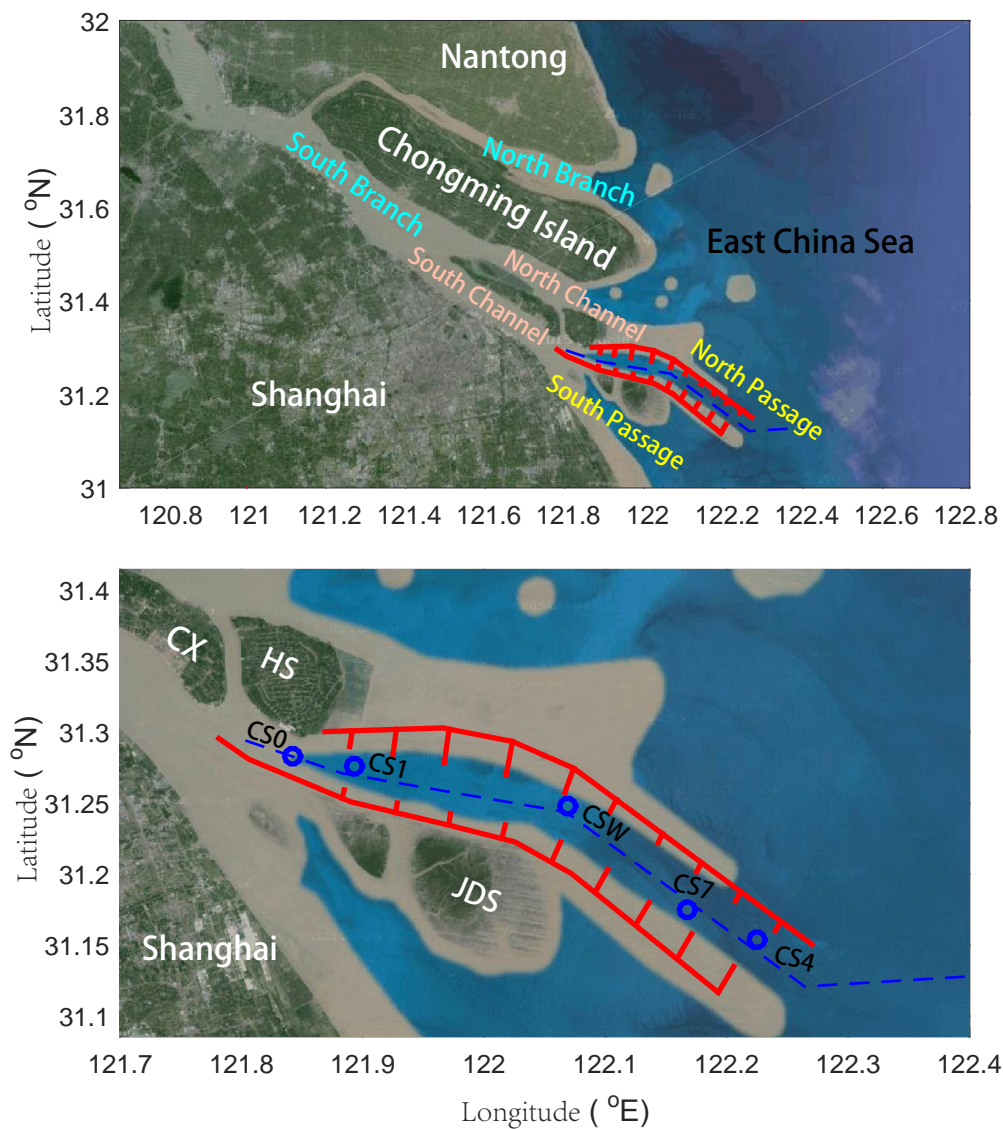


**Figure 1.** Sketch of the Yangtze River Estuary. CX, HS and JDS represent the Changxing Island, Hengsha Island and Jiuduansha Shoal. Blue circles are the locations of the gauging stations in the North Passage. The red lines represent the Northern and Southern dikes.

## 2.2. Numerical Model

The non-hydrostatic wave model (NHWAVE) has been implemented to solve the hydrodynamic and transport equation in this study. NHWAVE was developed by Ma et al. [40], which was originally utilized to simulate dispersive waves and tsunamis. Ma et al. [41] extended the application of NHWAVE by considering the baroclinic pressure forcing in the momentum equation. To decrease the time consumed in solving the Poisson equation, Shi et al. [42] added a pressure decimation interpolation (PDI) method into NHWAVE, which can greatly improve the model’s efficiency without significantly impacting the model’s accuracy obviously.

### 2.2.1. Governing Equations

NHWAVE is a parallelized model based on the incompressible Navier-Stokes equations in  $\sigma$  coordinate system. The continuity and momentum equations are written as

$$\frac{\partial D}{\partial t} + \frac{\partial Du}{\partial x} + \frac{\partial Dv}{\partial y} + \frac{\partial \omega}{\partial \sigma} = 0 \tag{1}$$

$$\frac{\partial \mathbf{U}}{\partial t} + \frac{\partial \mathbf{F}}{\partial x} + \frac{\partial \mathbf{G}}{\partial y} + \frac{\partial \mathbf{H}}{\partial \sigma} = \mathbf{S}_h + \mathbf{S}_p + \mathbf{S}_\rho + \mathbf{S}_\tau \tag{2}$$

where  $D$  is the total water depth.  $\mathbf{U} = (Du, Dv, Dw)^T$ ,  $(u, v, w)$  are velocities in  $(x, y, z)$  directions.  $\mathbf{F}, \mathbf{G}, \mathbf{H}$  represent fluxes terms.  $\mathbf{S}_h, \mathbf{S}_p, \mathbf{S}_\rho, \mathbf{S}_\tau$  are source terms, which include the bottom slope term, dynamic pressure gradient, baroclinic forcing and turbulent mixing term derived from the Boussinesq approximation, respectively.  $\omega$  is the vertical velocity in  $\sigma$ -coordinates, which can be given by

$$\omega = \left(\frac{\partial h}{\partial t} - \sigma \frac{\partial D}{\partial t}\right) + u\left(\frac{\partial h}{\partial x} - \sigma \frac{\partial D}{\partial x}\right) + v\left(\frac{\partial h}{\partial y} - \sigma \frac{\partial D}{\partial y}\right) + w\left(\frac{1}{D}\right) \tag{3}$$

To maintain the flux and source terms are automatically balanced in the steady state, the well balanced method [43,44], which can avoid artificial flow due to bottom slope, is adopted to treat the bed slope source term. Therefore, the source term can be written as

$$\mathbf{S}_h = \begin{pmatrix} g\eta \frac{\partial h}{\partial x} \\ g\eta \frac{\partial h}{\partial y} \\ 0 \end{pmatrix} \tag{4}$$

$$\mathbf{S}_p = \begin{pmatrix} -\frac{D}{\rho} \left(\frac{\partial p}{\partial x} + \frac{\partial p}{\partial \sigma} \frac{\partial \sigma}{\partial x^*}\right) \\ -\frac{D}{\rho} \left(\frac{\partial p}{\partial y} + \frac{\partial p}{\partial \sigma} \frac{\partial \sigma}{\partial y^*}\right) \\ -\frac{1}{\rho} \frac{\partial p}{\partial \sigma} \end{pmatrix} \tag{5}$$

$$\mathbf{S}_\rho = \begin{pmatrix} -gD \left(\frac{\partial r}{\partial x} + \frac{\partial r}{\partial \sigma} \frac{\partial \sigma}{\partial x^*}\right) \\ -gD \left(\frac{\partial r}{\partial y} + \frac{\partial r}{\partial \sigma} \frac{\partial \sigma}{\partial y^*}\right) \\ -g \frac{\partial r}{\partial \sigma} \end{pmatrix} \tag{6}$$

$$\mathbf{S}_\tau = \begin{pmatrix} DS_{\tau x} \\ DS_{\tau y} \\ DS_{\tau z} \end{pmatrix} \tag{7}$$

where the  $(x^*, y^*, z^*)$  are the Cartesian coordinate system.  $\eta$  represents surface elevation.  $p$  is the dynamic pressure.  $r$  is the baroclinic pressure head, which can be calculated by

$$r = \frac{D}{\rho_0} \int_{\sigma}^1 \rho d\sigma \tag{8}$$

where  $\rho_0$  is the constant reference density and  $\rho$  servers as the dynamic density with expression as  $\rho = \rho_m - \rho_0$ .  $\rho_m$  is the density of the mixture.

### 2.2.2. Numerical Approach

In the present version of NHWAVE, regular grids are used in horizontal directions, and the  $\sigma$  coordinate system is defined in vertical direction to represent bottom and surface geometry accurately. Following the Keller-box scheme proposed by Stelling and Zijlema [45], the velocities  $(u, v, w)$  are placed at the cell center, but the dynamic pressure ( $p$ ) is defined at the velocity-facing cell faces. This grid configuration can exactly set the free surface pressure to be zero and reduce error in calculating of dynamic pressure. Using the Keller-box scheme, non-hydrostatic models can simulate highly dispersive waves well with only 3–5 vertical layers.

The second-order Runge-Kutta scheme is adopted for time stepping to obtain second-order accuracy in NHWAVE. The momentum equation (Equation (2)) is discretized by a second-order

Godunov type finite volume method. The fluxes at the cell faces are estimated by HLL [46] or HLLC [47] approximate Riemann solvers. The pressure-correction projection method is adopted in NHWAVE to get the velocities at each time step, which divides the total pressure into two parts: dynamic pressure and hydrostatic pressure. In the first step, the intermediate values of velocities are calculated from the momentum equation without the dynamic term ( $S_p$ ). In the second step, the dynamic pressure can be obtained by solving the pressure Poisson equation, then, the velocities are corrected by the dynamic term. Therefore, the velocities at  $k$ th stage in Runge-Kutta scheme can be expressed as

$$u^{(k)} = u^* - \frac{\Delta t}{\rho} \left( \frac{\partial p}{\partial x} + \frac{\partial p}{\partial \sigma} \frac{\partial \sigma}{\partial x^*} \right)^{(k)} \tag{9}$$

$$v^{(k)} = v^* - \frac{\Delta t}{\rho} \left( \frac{\partial p}{\partial y} + \frac{\partial p}{\partial \sigma} \frac{\partial \sigma}{\partial y^*} \right)^{(k)} \tag{10}$$

$$w^{(k)} = w^* - \frac{\Delta t}{\rho} \frac{1}{D^{(k)}} \frac{\partial p^{(k)}}{\partial \sigma} \tag{11}$$

where  $u^*$  represents the intermediate value at the first step.

The pressure Poisson equation in  $(x, y, \sigma)$  coordinate system can be derived by substituting Equation (11) into the continuity equation (Equation (1)).

$$\frac{\partial}{\partial x} \left[ \frac{\partial p}{\partial x} + \frac{\partial p}{\partial \sigma} \frac{\partial \sigma}{\partial x^*} \right] + \frac{\partial}{\partial y} \left[ \frac{\partial p}{\partial y} + \frac{\partial p}{\partial \sigma} \frac{\partial \sigma}{\partial y^*} \right] + \frac{\partial}{\partial \sigma} \left( \frac{\partial p}{\partial x} \right) \frac{\partial \sigma}{\partial x^*} \tag{12}$$

$$+ \frac{\partial}{\partial \sigma} \left( \frac{\partial p}{\partial y} \right) \frac{\partial \sigma}{\partial y^*} + \left[ \left( \frac{\partial \sigma}{\partial x^*} \right)^2 + \left( \frac{\partial \sigma}{\partial y^*} \right)^2 + \frac{1}{D^2} \right] \frac{\partial}{\partial \sigma} \left( \frac{\partial p}{\partial \sigma} \right) \tag{13}$$

$$= \frac{\rho}{\Delta t} \left( \frac{\partial u^*}{\partial x} + \frac{\partial u^*}{\partial \sigma} \frac{\partial \sigma}{\partial x^*} + \frac{\partial v^*}{\partial y} + \frac{\partial v^*}{\partial \sigma} \frac{\partial \sigma}{\partial y^*} + \frac{1}{D} \frac{\partial w^*}{\partial \sigma} \right) \tag{14}$$

Assuming strong vertical mixing, the turbulence closure proposed by Pacanowski and Philander [48] was used. The  $\nu_z$  is calculated from

$$\nu_z = \frac{\nu_1}{(1 + \alpha Ri)^n} + \nu_0 \tag{15}$$

where  $\nu_0 = 10^{-3} \text{ m}^2/\text{s}$  is the background dissipation parameters and  $\nu_1 = 1.5 \times 10^{-2} \text{ m}^2/\text{s}$ ,  $\alpha = 5$ ,  $n = 2$  are adjustable parameters [49].  $Ri$  is the Richardson number.

### 2.3. Model Setup

Bathymetry was obtained from a field survey along North Passage in February 2009. The horizontal grid spacing is set to be 2.5 m and 40 layers in the vertical direction were used. The simulation begins on 7:00 27 April 2009 UTC and ends on 19:30 27 April 2009 UTC. The model is forced by the observed velocities at the left boundary and by sea level at the right boundary. As there are only 5 gauge stations along the North Passage which cannot provide enough information to well represent the initial state, the initial conditions of the salinity and velocity fields are extracted by the model established by Lu et al. [34] with consideration of baroclinic forcing.

At the surface, a free-slip boundary is applied. At the bottom, the effect of bottom friction is considered with the roughness height being set to be 0.001 m. The time step ( $\Delta t$ ) is adaptive during the simulation using the Courant-Friedrichs-Lewy (CFL) criterion

$$\Delta t = CFL \min \left[ \min \frac{\Delta x}{|u_{i,j,k}| + \sqrt{gD_{i,j}}}, \min \frac{\Delta y}{|v_{i,j,k}| + \sqrt{gD_{i,j}}}, \min \frac{\Delta \sigma D_{i,j}}{|w_{i,j,k}|} \right] \tag{16}$$

where  $C$  is the Courant number.

### 3. Model Results

The North Passage can be divided into three parts: the Upper Reach, the Middle Reach and the Lower Reach. The Upper Reach begins at CS0 with the length of 28.6 km. The Middle Reach is between 5km above and lower station CSW. The Lower Reach is from the lower end of the Middle Reach to station CS4. As shown in Figure 1, stations CS1, CSW and CS7 are gauge stations in the Upper, Middle and Lower Reaches, respectively. The numerical results are compared with the observed water level, velocity and salinity data at the three stations.

Figure 2 compares predicted sea level at the three gauge stations with observations. The model accurately capture the oscillating sea level. Both the phase and amplitude are simulated well in the whole channel. At station CS7, the model shows an excellent agreement with the observation. At the other two stations, a slight discrepancy occurs during the ebb tide. As the simulation is based on a vertical 2D domain, it cannot provide results representing the tidal distortion and asymmetry induced by the geometry of the North Passage.

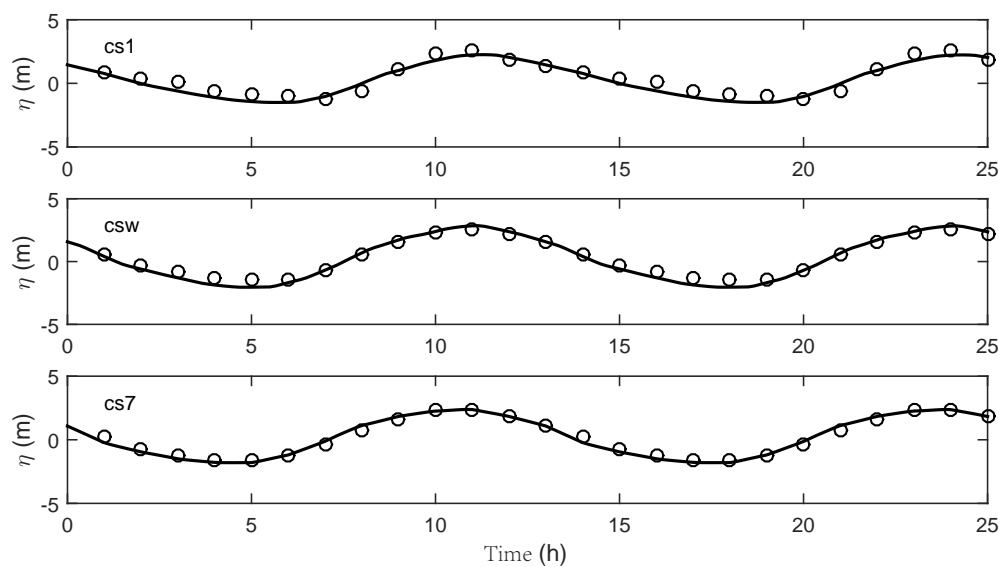


**Figure 2.** Comparisons of sea level between predicted values (Solid lines) and observations (Cycles) at CS1, CSW and CS7 within the North Passage.

Velocity and salinity measurements were made at six different relative water depths  $h/H = 0.0, 0.2, 0.4, 0.6, 0.8$  and  $1.0$  (where  $h$  is defined as the vertical distance from the bottom and  $H$  is the whole water depth.  $0.0$  means the bottom and  $1.0$  refers to the free surface). Figures 3–5 shows the comparisons of velocity and salinity at CS1, CSW and CS7 respectively. Overall, the magnitudes of velocity are well predicted by the model. The model can predict the variations of vertical distributions of velocity with good accuracy. However, the comparison also shows some discrepancies near the bed. It might be induced by the constant bottom roughness used in the model. In the North Passage, the bottom friction can be impacted by the bottom material and topography.

Figures 3–5 also depicts the vertical distributions of salinity at CS1, CSW and CS7. The accurate prediction of salinity is a more difficult than that of surface water level and velocity. The model overestimate the salinity near bottom st CS7 from  $t = 9$  to  $11$  h. This might due to the overestimation of the inflow from the right boundary during flood tide. Evidence can be found in Figure 5 that the model slightly overestimates the velocity during this period.

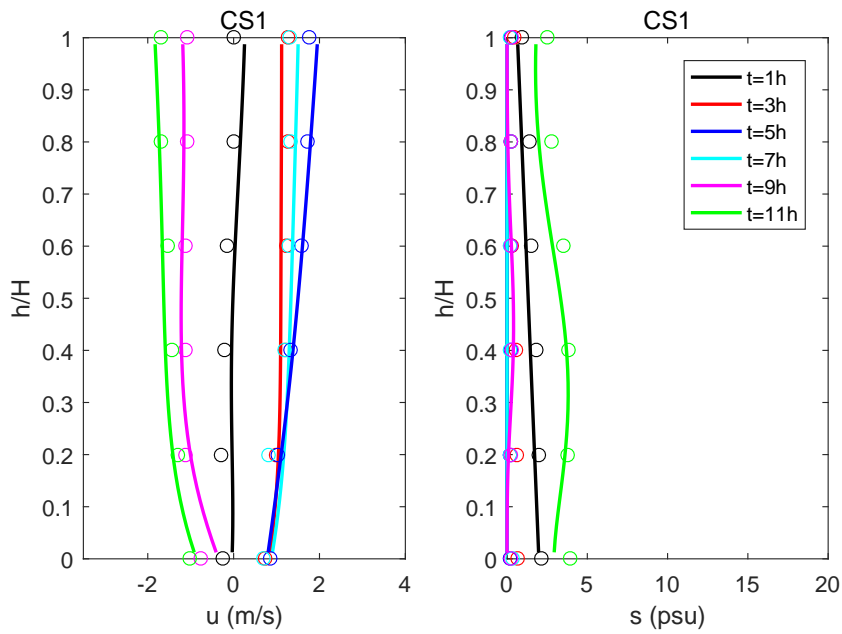


**Figure 3.** Comparison of current speed ( $u$ ) and salinity ( $s$ ) at CS1. (Solid lines: predicted results; Circles: observations).

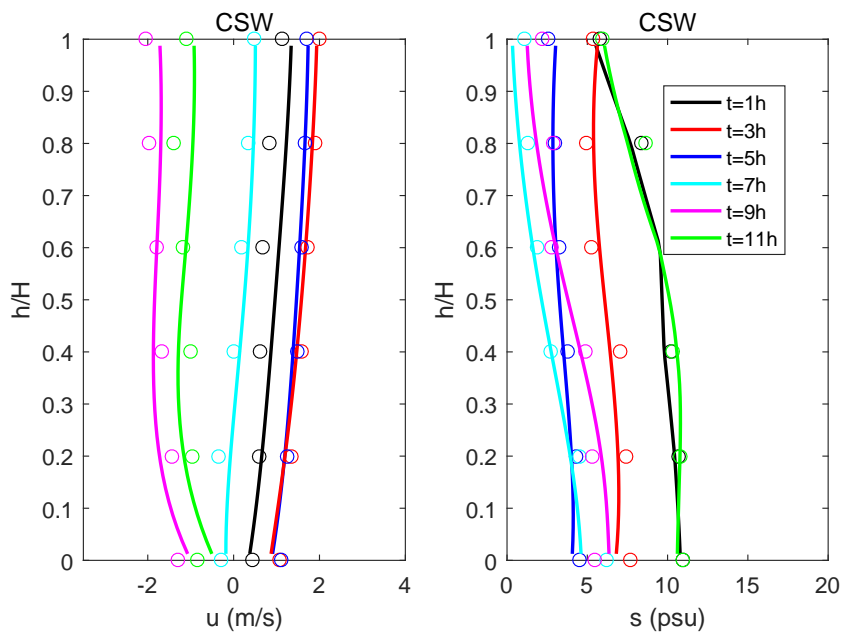


**Figure 4.** Comparison of current speed ( $u$ ) and salinity ( $s$ ) at CSW. (Solid lines: predicted results; Circles: observations).

These results show that the non-hydrostatic model can capture the qualitative features of the hydrodynamics in the North Passage over a full tidal cycle. Further improvements, such as more reasonable bottom roughness used in numerical modelling, are needed to be carried out for better prediction. However, these improvement methods are out the scope of this paper, and the discrepancies do not greatly impact the analysis of K-H instability. The discussion of the K-H billow characteristics will be focused on in the following sections.

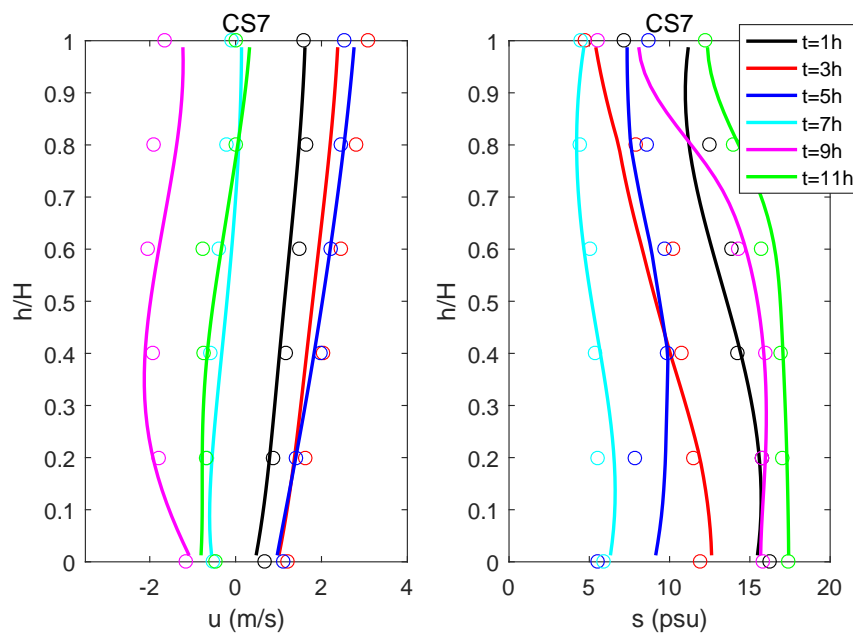


**Figure 5.** Comparison of current speed ( $u$ ) and salinity ( $s$ ) at CS7. (Solid lines: predicted results; Circles: observations).

#### 4. Discussion

YRE is a mesotidal, partially-mixed estuary. The periodic stratification and mixing, induced by the interaction of tidal currents and freshwater discharge, can greatly impact the estuarine environment. During the process from stratification to mixing, K-H instability is a critical mechanism for turbulence development [21]. However, both the spatial and temporal resolutions of the observations are too coarse to observe K-H instabilities in this area. Pu et al. [39] found that the K-H instability might exist within the middle and lower reaches of the North Passage. To validate the existence of K-H instability, the numerical results are used to analyze salinity and velocity fields within the North Passage.

##### 4.1. The Existence of K-H Instability

The value of  $Ri < 0.25$  is necessary for the occurrence of K-H instability, but it is not sufficient. Thus, this criterion can only be used to analyze the possibility of K-H instability, but cannot detect the occurrence of K-H instability. K-H billows are the direct manifestation of the existence of K-H instability. Therefore, the distributions of the salinity are plotted and used to evaluate the existence of K-H billows. Figure 6 shows the spatial distributions of salinity at  $t = 7.2, 8.2$  and  $9.2$  h, respectively. Perturbations can be noticed, which occurs in the vicinity of the pycnocline. The intensity of the perturbations increases as the saltwedge moves to upstream from  $t = 7.2$  to  $8.2$  h, then, decreases from  $8.2$  to  $9.2$  h. The perturbations experience their strongest intensity at  $t = 8.2$  h. The figure also shows the perturbations is not only vigorous enough to mix the fluid around pycnocline, but also cause mixing in the whole vertical domain at  $x = 49 - 51$  km. In the lower panel of Figure 6, the intensity of the perturbations have greatly decreased, indicating the duration of the perturbations of salinity is approximate 2 h.

Figure 7 is a zoom-in of the distribution of salinity at  $t = 7.2$  h. The figure reveals a train of K-H billows around the pycnocline at  $50.8-51$  km downstream of station CS0. The billows are approximately  $50-60$  m long and  $6$  m high. The generation of the billows is induced by the sheared flow within the density interface. The occurrence of K-H billows is associated with strong salinity gradients and shears across the pycnocline. The corresponding values of  $N^2$ ,  $S^2$  and  $Ri$  along the dashed line in Figure 7a are calculated and shown in Figure 7b-d. The value of  $S^2$  confirms that the shear is strong at the positions

where K-H billows exist. The maximum value of  $N^2$  are also at the density interface. The generation of the billows is induced by the sheared flow within the density interface.

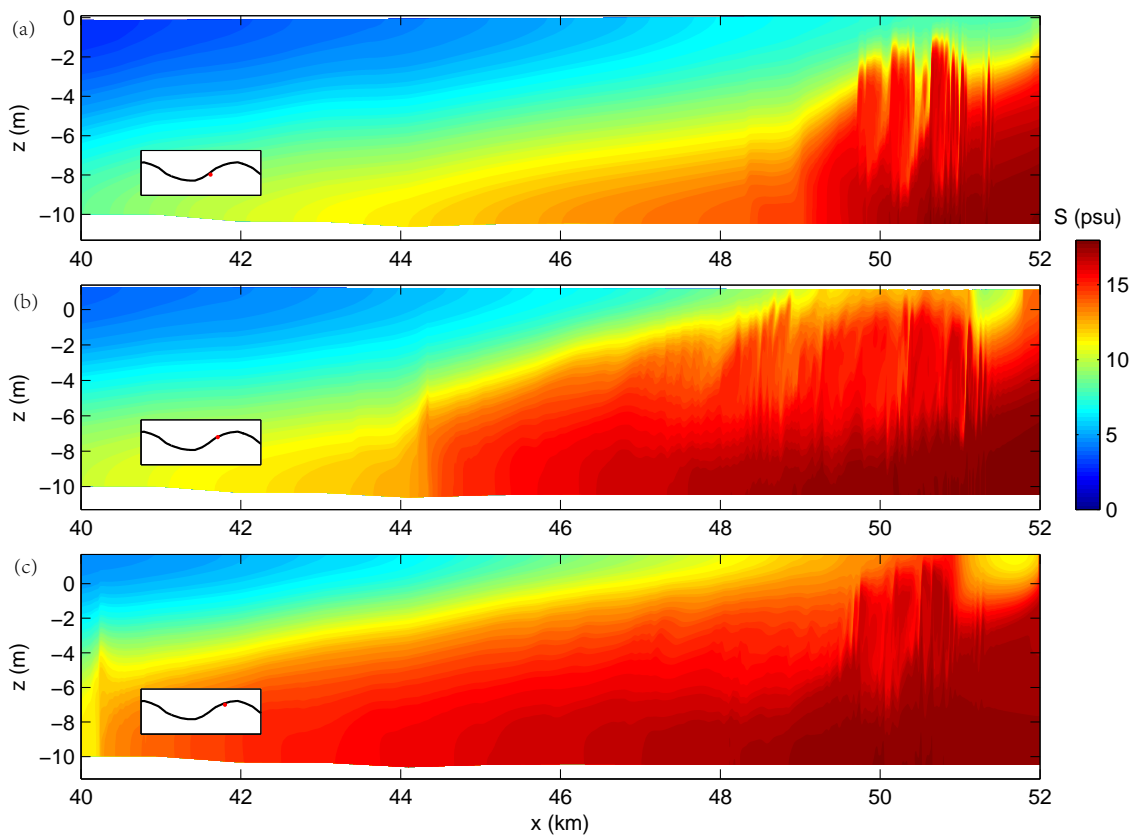


Figure 6. Spatial distributions of salinity at (a)  $t = 7.2$  h; (b)  $t = 8.2$  h; (c)  $t = 9.2$  h.

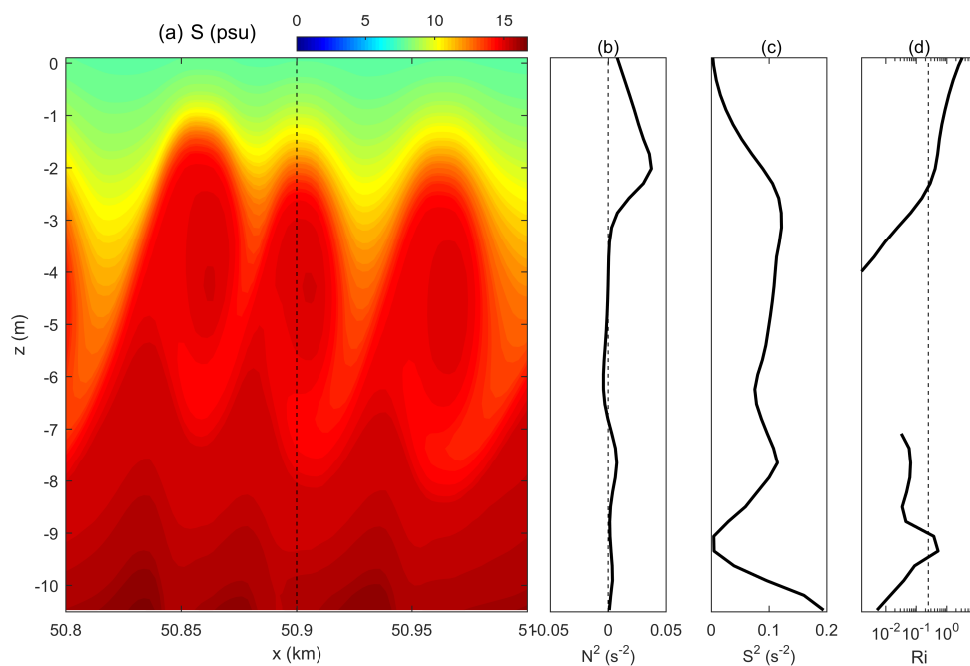


Figure 7. Vertical distributions of (a) salinity, (b) the Brunt-Väisälä frequency ( $N^2$ ), (c) the velocity shear ( $S^2$ ) and (d) Richardson number ( $Ri$ ) at  $t = 7.2$  h. (Dashed line in (a) represents the location for calculating  $N^2$ ,  $S^2$  and  $Ri$ ; Dashed line in (d) means  $Ri = 0.25$ ).

#### 4.2. The Spatial and Temporal Scales of the K-H Billows

The horizontal size of the billows is estimated by calculating the spectral representation of the resolved flow field at  $t = 7.2$  h. The Fast Fourier Transform (FFT) is employed to transform the vertical velocity distribution into the spectral field. The expression of FFT can be given by

$$w(x, z) = \sum_{n=-N+1}^N \hat{w}_n(k_x, z) e^{ik_x x} \quad (17)$$

where  $k_x = 2\pi/L$  is the wave number,  $L$  is wave length,  $\hat{w}_n$  is the Fourier coefficient,  $N$  is the half number of the grid in the  $x$  direction. To get the relative importance of the various spectral components, we normalize the spectrum by the following equation:

$$P(n, z) = \frac{|\hat{w}_n|^2}{\sum_{n=-N+1}^N |\hat{w}_n|^2} \quad (18)$$

The averaged wave number ( $\bar{k}_x$ ) can be expressed as

$$\bar{k}_x = \sum_{n=-N+1}^N P(n, z) k_x(n) \quad (19)$$

At  $t = 7.2$  h, the K-H instability mainly occurs at  $x = 49$ – $51$  km. Therefore, we choose the streamwise distance ranging from 49 to 51 km to calculate the spectrum. The representative depth is chosen at the center of the K-H billows, which is at  $z = -5$  m. Figure 8 depicts the normalized spectral density of the vertical velocity. It can be seen that the maximum value of the spectrum locates at  $k_x = 0.1 \text{ m}^{-1}$ , which corresponds to the billows with horizontal length of 62.8 m. The main energy is in wave numbers  $k_x = 0$  to  $0.2 \text{ m}^{-1}$ . The averaged wave number is  $0.105 \text{ m}^{-1}$ , thus, the mean horizontal size of the billows at  $x = -5$  m is 59.8 m. To get the averaged billow size over depth, we calculated the averaged wave number from  $z = -2$  to  $-9$  m. The vertical distribution of averaged wave number is shown in Figure 9. The wave number, which shows a maximum at  $z = -7.8$  m, corresponds to the horizontal size of 56–61 m. The calculated length scale is consistent with the observations at the Fraser River Estuary conducted by Tedford et al. [22]. In their observation, they also found that the length scale of the billows was impacted by incoming tidal waves and river discharges. To investigate the range of the length scale during our simulation, we calculate the averaged wave number at time between from 7 h and 10 h at 5 min intervals for  $x \in [49, 51]$  km. The wave length of K-H billows ranges between 59 m and 83 m (See Figure 10). At the beginning of the occurrence of the K-H billows from  $t = 7$ – $8.2$  h, the structure of the billows is relatively regular with wave length of approximate 60 m. Then, the wave length increases with decreasing intensity of the K-H instability. The maximum wave length is 83 m, which occurs at  $t = 9.8$  h.

The generation and evolution of the billows can be seen in Figure 11. The figures are plotted in 150 s interval. In the first 150 s, forced by the sheared flow, K-H billows arise from the perturbations at the salinity interface. The structures of the billows are well described by the model. Then, the billows extend the shapes both in horizontal and vertical direction, but the braids between the billows become unobvious. Finally, in Figure 11d, the structures of the billows cannot be recognized, and the stratified flow is well mixed. Therefore, the K-H billows last for about 6 min, which is consistent with the observations of Chang et al. [23].

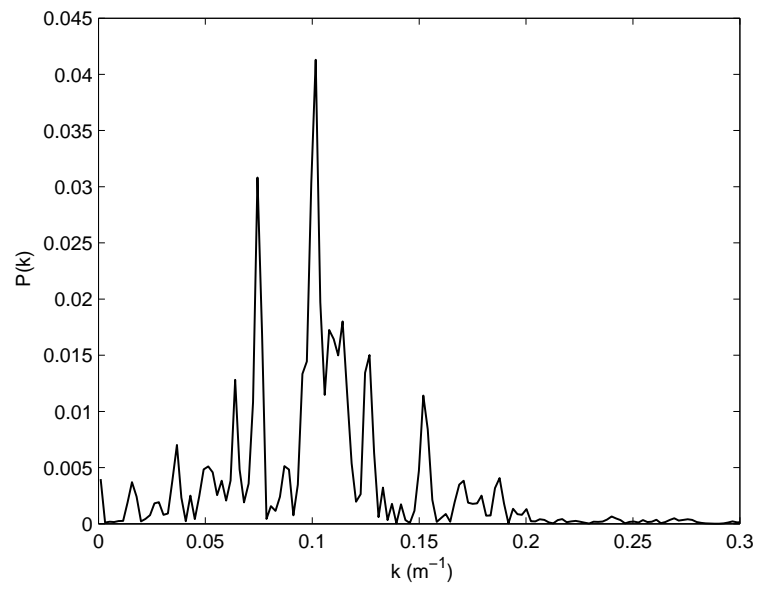


Figure 8. The normalized spectral density  $t = 7.2$  h,  $z = -5$  m.

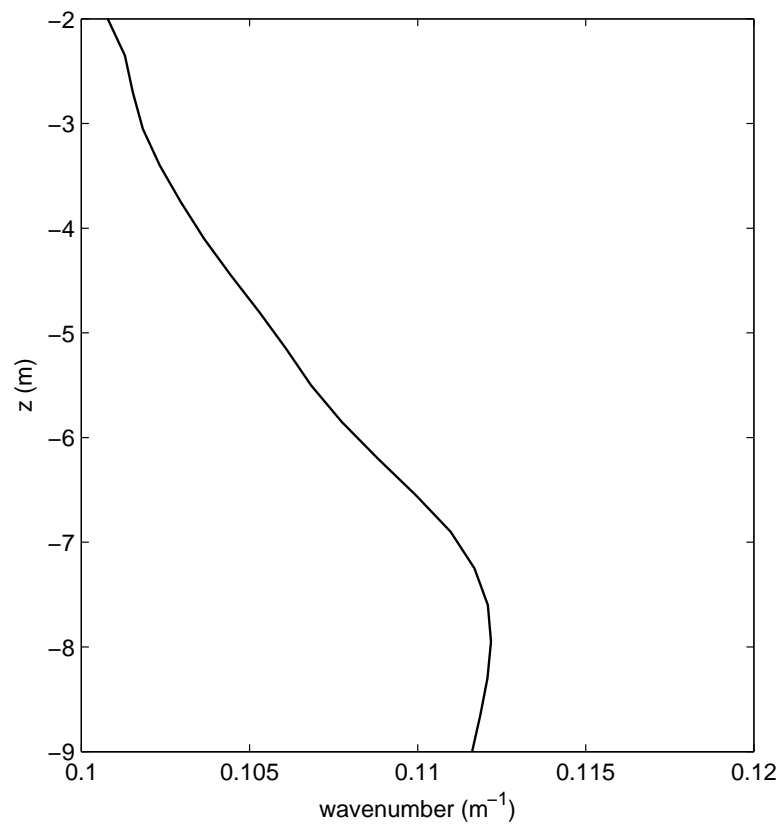
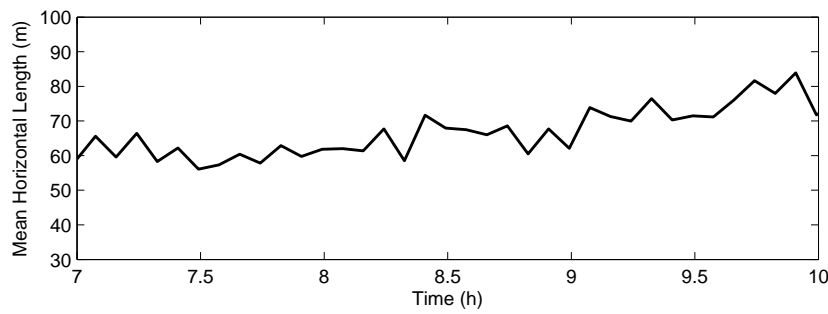
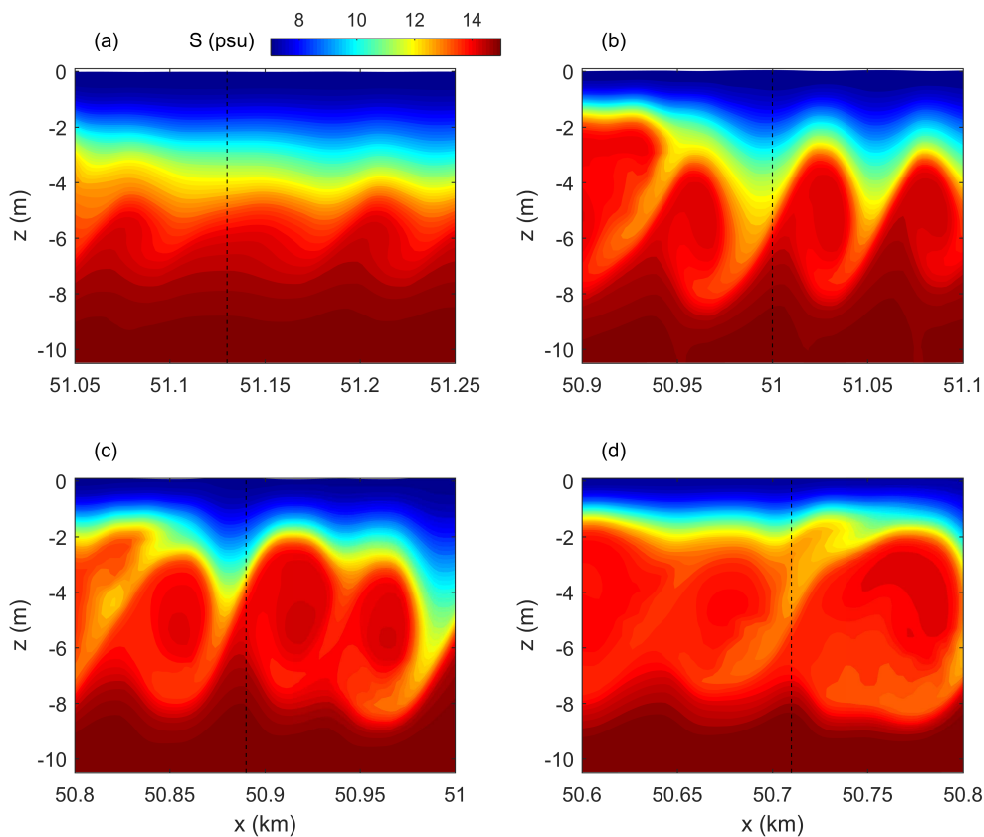


Figure 9. The averaged wavenumber as a function of vertical location at  $t = 7.2$  h.



**Figure 10.** Time series of the mean horizontal length scale of the K-H billows.



**Figure 11.** Generation and evolution of the billows ((a)  $t = 7.117$  h; (b–d) are taken 2.5, 5 and 7.5 min after (a); the dashed lines indicate the locations of the same billow).

### 4.3. Mixing Efficiency

In this section, the effects of K-H instability on mixing efficiency is considered. The spatial distributions of the salinity, velocities and vorticity at  $t = 7.2$  h are plotted in Figure 12. A trains of K-H billows are clearly shown in Figure 12a. There is an obvious shear layer in the vicinity of the pycnocline. At the locations of the billows, the surface horizontal velocity seems to be smaller than the surrounding values. The distribution of vertical velocity shows a remarkable difference at the locations where the billows exist. The K-H instability has greatly accelerated the vertical exchange, and the maximum magnitude of  $w$  is around 0.08 m/s. Figure 12d depicts the distribution of spanwise vorticity ( $\omega_y$ ). It can be seen the large values of  $\omega_y$  are within the braids. According to Corcos and Sherman [50], the secondary instability of spanwise vorticity within the braid plays an essential role in mixing at high Reynolds number ( $Re$ ). In this case, the  $Re$  can be calculated by

$$Re = u\delta/\nu \tag{20}$$

where  $u$  is half the velocity difference across the shear layer,  $\delta$  is the half-width of the shear zone, and  $\nu$  is the kinematic viscosity of the fluid. We estimate the value of  $Re$  at  $t = 7.2$  h, which is approximate 500,000. This value is similar to the observation which shows K-H billows in Geyer et al. [21]. The result of intensive values of  $\omega_y$  within the braid is also consistent with the observations, which demonstrates the present numerical model can capture the evolution of K-H billows at high  $Re$ .

The amount of mixing rate is estimated by calculating the changes in gravitational potential energy. The relative mixing rate ( $M_r$ ) is adopted, which is given by,

$$M_r = \frac{dP_{PE}/dt}{P_{PE}} \tag{21}$$

where  $P_{PE} = (g/A_b) \int_V \rho(x, z, t)z dV$  is the potential energy per horizontal area [51,52].  $A_b$  and  $V$  are the horizontal area and volume for the distribution of the density field  $\rho(x, z, t)$ .

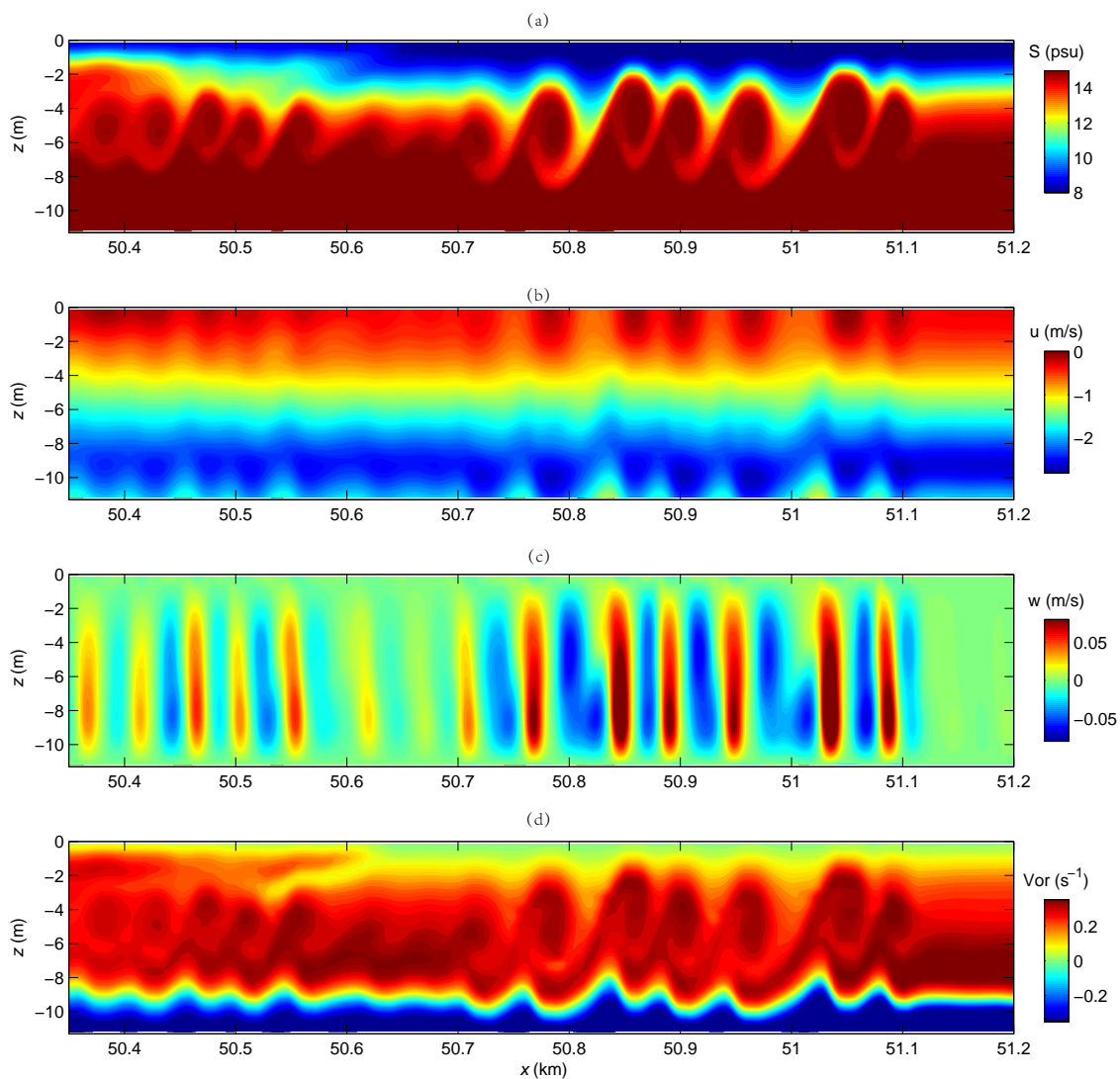


**Figure 12.** Distributions of (a) salinity, (b) streamwise velocity( $u$ ), (c) vertical velocity ( $w$ ) and (d) spanwise vorticity at  $t = 7.2$ h.

The  $M_r$  during the predicted tidal cycle is shown in Figure 13. Again, the values at  $x = 50, 48$  and  $46$  km are shown to analyze the influence of K-H instability on mixing. It is shown that  $M_r$  has a notable ebb-flood variation, especially at  $x = 50$  and  $48$  km. During ebb tide, the changes of the potential energy at the three selected locations seem to be same. Due to the heavy salt water moves

seaward, the potential energy decreases during ebb, which leads to a negative value of  $M_r$ . After that the value of  $M_r$  increases from the beginning of flood. The value of  $M_r$  at  $x = 46$  km is slightly larger than 0 during flood. However, the values show perturbations at the other two points during flood tide, which correspond to the existence of K-H billows. The value of  $M_r$  during the existence of K-H billows is much larger than the corresponding values at other period. The maximum value of  $M_r$  at  $x = 50$  km occurs at  $t = 7.2\text{--}7.5$  h with maximum value of  $M_r = 5 \times 10^{-6} \text{ Jm}^{-2}\text{s}^{-1}$ . The perturbations of  $M_r$  confirm that the K-H instability can improve the mixing efficiency and the mixing mainly occurs in the lower reach due to the existence of K-H instability.

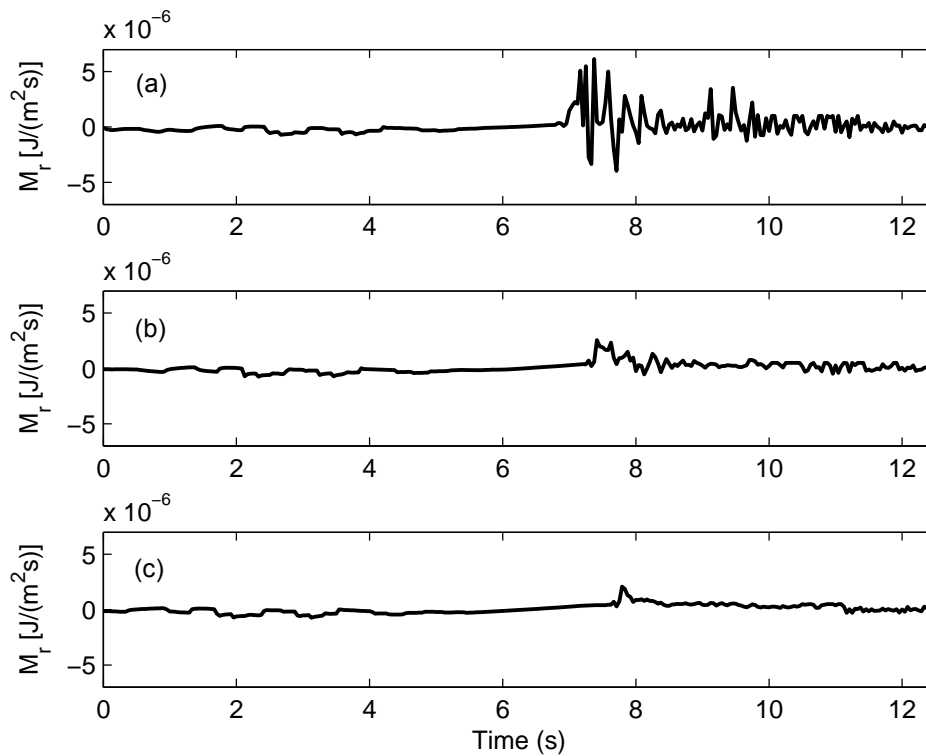


**Figure 13.** Time series of the mixing rate ( $M_r$ ) at  $x = 50$  km (a),  $x = 48$  km (b) and  $x = 46$  km (c).

### 5. Conclusions

In this study, a high resolution non-hydrostatic model has been employed to explore the existence of K-H instability in the North Passage of YRE. The spacial grid is set to be 2.5 m to capture the evolution of K-H billows.

The model can capture the existence of K-H instability during flood tide. The instability occurs 48-51 km downstream of station CS0 (See Figure 1). The duration and intensity of K-H instability decreases from  $x = 51$  to 48 km. The horizontal length scale of the K-H billows experiences a stable period from  $t = 7.2$  to 8.2 h, with lengths of approximately 60 m, in agreement with the field observations by Tedford et al. [22]. Therefore, the wavelength increases with the decrease of the K-H instability intensity. The K-H billows have vertical scales of 6–7 m and time scales of 6 min. The changes of potential energy is adopted to estimate the mixing efficiency. The mixing rate shows perturbations during the existence of K-H instability, which indicates intensive vertical mixing induced by K-H instability. The values of  $M_r$  show a significant increase during the generation of the K-H instability because the K-H instability can greatly increase the mixing efficiency.

**Author Contributions:** J.S., C.T. and J.Z. conceived and wrote the paper draft. J.S. performed the numerical simulations. C.Z. and X.G. contributed to the analysis and discussion of the results. C.Z. and J.Z. revised the paper. J.S. and C.T. revised the simulations and updated the paper according to their review.

**Funding:** This work was supported by the National Key R&D Program of China (2017YFC0405402, 2017YFC0405401), the National Natural Science Foundation of China (41706087, 51879096), the National Science Foundation for Distinguished Young Scholars (51425901), the Natural Science Foundation of Jiangsu Province (Grant No. BK20170867, BK20161509), Marine Science and Technology Innovation Project of Jiangsu Province (HY2018-15), the Fundamental Research Funds for the Central Universities(2017B2151, 2018B653X14), the Key Laboratory of Water-Sediment Sciences and Water Disaster Prevention of Hunan Province (2018SS02), Postgraduate Research & Practice Innovation Program of Jiangsu Province(KYCX18\_0613).

**Acknowledgments:** The authors would like to acknowledge Experimental Center in College of Harbour, Coastal and offshore Engineering, Hohai University. Numerical simulations were performed on Community Cluster of the Experimental Center.

**Conflicts of Interest:** The authors declare no conflict of interest.

## References

- Hu, K.; Ding, P.; Wang, Z.; Yang, S. A 2D/3D hydrodynamic and sediment transport model for the Yangtze Estuary, China. *J. Mar. Syst.* **2009**, *77*, 114–136. [[CrossRef](#)]
- Zheng, J.; Zhang, C.; Demirebilek, Z.; Lin, L. Numerical study of sandbar migration under wave-undertow interaction. *J. Waterw. Port Coast. Ocean Eng.* **2014**, *140*, 146–159. [[CrossRef](#)]
- Zhang, C.; Zhang, Q.; Zheng, J.; Demirebilek, Z. Parameterization of nearshore wave front slope. *Coast. Eng.* **2017**, *127*, 80–87. [[CrossRef](#)]
- Horner-Devine, A.R.; Hetland, R.D.; MacDonald, D.G. Mixing and transport in coastal river plumes. *Annu. Rev. Fluid Mech.* **2015**, *47*, 569–594. [[CrossRef](#)]
- Shi, J.; Zheng, J.; Tong, C. Non-hydrostatic modelling of Kelvin-Helmholtz billows along the North Passage of Yangtze River Estuary, China. *Coast. Eng. Proc.* **2018**, *1*, 81. [[CrossRef](#)]
- Chen, W.Y.; Chen, G.X.; Chen, W.; Liao, C.C.; Gao, H.M. Numerical simulation of the nonlinear wave-induced dynamic response of anisotropic poro-elastoplastic seabed. *Mar. Georesour. Geotechnol.* **2018**, 1–12. [[CrossRef](#)]
- Liao, C.; Tong, D.; Jeng, D.S.; Zhao, H. Numerical study for wave-induced oscillatory pore pressures and liquefaction around impermeable slope breakwater heads. *Ocean Eng.* **2018**, *157*, 364–375. [[CrossRef](#)]
- Thomson, W. Hydrokinetic solutions and observations. *Philos. Mag.* **1871**, *42*, 362–377. [[CrossRef](#)]
- Von Helmholtz, H. Die energie der wogen und des windes. *Ann. Phys.* **1890**, *277*, 641–662. [[CrossRef](#)]
- Miles, J.W. On the stability of heterogeneous shear flows. *J. Fluid Mech.* **1961**, *10*, 496–508. [[CrossRef](#)]
- Howard, L.N. Note on a paper of John W. Miles. *J. Fluid Mech.* **1961**, *10*, 509–512. [[CrossRef](#)]
- Hazel, P. Numerical studies of the stability of inviscid parallel shear flows. *J. Fluid Mech.* **1972**, *39*, 39–61.
- Fringer, O.B.; Street, R.L. The dynamics of breaking progressive interfacial waves. *J. Fluid Mech.* **2003**, *494*, 319–353. [[CrossRef](#)]
- Barad, M.F.; Fringer, O.B. Simulations of shear instabilities in interfacial gravity waves. *J. Fluid Mech.* **2010**, *644*, 61–95. [[CrossRef](#)]
- Fructus, D.; Carr, M.; Grue, J.; Jensen, A.; Davies, P.A. Shear-induced breaking of large internal solitary waves. *J. Fluid Mech.* **2009**, *620*, 1–29. [[CrossRef](#)]
- Troy, C.D.; Koseff, J.R. The instability and breaking of long internal waves. *J. Fluid Mech.* **2005**, *543*, 107–136. [[CrossRef](#)]
- Woods, J.D. Wave-induced shear instability in the summer thermocline. *J. Fluid Mech.* **1968**, *32*, 791–800. [[CrossRef](#)]
- Geyer, W.R.; Smith, J.D. Shear instability in a highly stratified estuary. *J. Phys. Oceanogr.* **1987**, *17*, 1668–1679. [[CrossRef](#)]
- Geyer, W.R.; Farmer, D.M. Tide-induced variation of the dynamics of a salt wedge estuary. *J. Phys. Oceanogr.* **1989**, *19*, 1060–1072. [[CrossRef](#)]
- Bourgault, D.; Saucier, F.J.; Lin, C.A. Shear instability in the St. Lawrence Estuary, Canada: A comparison of fine-scale observations and estuarine circulation model results. *J. Geophys. Res. Oceans* **2001**, *106*, 9393–9409. [[CrossRef](#)]
- Geyer, W.R.; Lavery, A.C.; Scully, M.E.; Trowbridge, J.H. Mixing by shear instability at high Reynolds number. *Geophys. Res. Lett.* **2010**, *37*, L22607. [[CrossRef](#)]
- Tedford, E.W.; Carpenter, J.R.; Pawlowicz, R.; Pieters, R.; Lawrence, G.A. Observation and analysis of shear instability in the Fraser River estuary. *J. Geophys. Res. Oceans* **2009**, *114*, C11006. [[CrossRef](#)]

23. Chang, M.H.; Jheng, S.Y.; Lien, R.C. Trains of large Kelvin-Helmholtz billows observed in the Kuroshio above a seamount. *Geophys. Res. Lett.* **2016**, *43*, 8654–8661. [[CrossRef](#)]
24. Marmorino, G.O. Observations of small-scale mixing processes in the seasonal thermocline, Part II: Wave breaking. *J. Phys. Oceanogr.* **1987**, *17*, 1348–1355. [[CrossRef](#)]
25. Lavery, A.C.; Chu, D.; Moum, J.N. Measurements of acoustic scattering from zooplankton and oceanic microstructure using a broadband echosounder. *J. Mar. Sci.* **2009**, *67*, 379–394. [[CrossRef](#)]
26. Shchepetkin, A.F.; McWilliams, J.C. The regional oceanic modeling system (ROMS): A split-explicit, free-surface, topography-following-coordinate oceanic model. *Ocean Model.* **2005**, *9*, 347–404. [[CrossRef](#)]
27. Chen, X. A fully hydrodynamic model for three-dimensional, free-surface flows. *Int. J. Numer. Methods Fluids* **2003**, *42*, 929–952. [[CrossRef](#)]
28. Stelling, G.W. *On the Construction of Computational Methods for Shallow Water Flow Problems*; Technical Report 35; Rijkwaterstaat: Dutch, The Netherlands, 1984.
29. Stelling, G.W. Practical aspects of accurate tidal computations. *J. Hydraul. Eng.* **1986**, *112*, 802–817. [[CrossRef](#)]
30. Özgökmen, T.M.; Johns, W.E.; Peters, H.; Matt, S. Turbulent mixing in the Red Sea outflow plume from a high-resolution nonhydrostatic model. *J. Phys. Oceanogr.* **2003**, *33*, 1846–1869. [[CrossRef](#)]
31. Wang, B.; Fringer, O.B.; Giddings, S.N.; Fong, D.A. High-resolution simulations of a macrotidal estuary using SUNTANS. *Ocean Model.* **2009**, *28*, 167–192. [[CrossRef](#)]
32. Fringer, O.; Gerritsen, M.; Street, R. An unstructured-grid, finite-volume, nonhydrostatic, parallel coastal ocean simulator. *Ocean Model.* **2006**, *14*, 139–173. [[CrossRef](#)]
33. Vlasenko, V.; Stashchuk, N.; McEwan, R. High-resolution modelling of a large-scale river plume. *Ocean Dyn.* **2013**, *63*, 1307–1320. [[CrossRef](#)]
34. Lu, S.; Tong, C.; Lee, D.Y.; Zheng, J.; Shen, J.; Zhang, W.; Yan, Y. Propagation of tidal waves up in Yangtze Estuary during the dry season. *J. Geophys. Res. Oceans* **2015**, *120*, 6445–6473. [[CrossRef](#)]
35. Shi, Z.; Li, C.; Dou, X. Three-dimensional modeling of tidal circulation within the north and south passages of the partially-mixed Changjiang River Estuary, China. *J. Hydrodyn.* **2010**, *22*, 656–661. [[CrossRef](#)]
36. Li, L.; Zhu, J.; Wu, H. Impacts of wind stress on saltwater intrusion in the Yangtze Estuary. *Sci. China Earth Sci.* **2012**, *55*, 1178–1192. [[CrossRef](#)]
37. Li, L.; He, Z.; Xia, Y.; Dou, X. Dynamics of sediment transport and stratification in Changjiang River Estuary, China. *Estuarine. Coast. Shelf Sci.* **2018**, *213*, 1–17. [[CrossRef](#)]
38. Zhang, M.; Townend, I.; Cai, H.; He, J.; Mei, X. The influence of seasonal climate on the morphology of the mouth-bar in the Yangtze Estuary, China. *Cont. Shelf Res.* **2018**, *153*, 30–49. [[CrossRef](#)]
39. Pu, X.; Shi, J.Z.; Hu, G.D.; Xiong, L.B. Circulation and mixing along the North Passage in the Changjiang River estuary, China. *J. Mar. Syst.* **2015**, *148*, 213–235. [[CrossRef](#)]
40. Ma, G.; Shi, F.; Kirby, J.T. Shock-capturing non-hydrostatic model for fully dispersive surface wave processes. *Ocean Model.* **2012**, *43–44*, 22–35. [[CrossRef](#)]
41. Ma, G.; Kirby, J.T.; Shi, F. Numerical simulation of tsunami waves generated by deformable submarine landslides. *Ocean Model.* **2013**, *69*, 146–165. [[CrossRef](#)]
42. Shi, J.; Shi, F.; Kirby, J.T.; Ma, G.; Wu, G.; Tong, C.; Zheng, J. Pressure Decimation and Interpolation (PDI) method for a baroclinic non-hydrostatic model. *Ocean Model.* **2015**, *96*, 265–279. [[CrossRef](#)]
43. Shi, F.; Kirby, J.T.; Harris, J.C.; Geiman, J.D.; Grilli, S.T. A high-order adaptive time-stepping TVD solver for Boussinesq modeling of breaking waves and coastal inundation. *Ocean Model.* **2012**, *43*, 36–51. [[CrossRef](#)]
44. Liang, Q.; Marche, F. Numerical resolution of well-balanced shallow water equations with complex source terms. *Adv. Water Resour.* **2009**, *32*, 873–884. [[CrossRef](#)]
45. Stelling, G.; Zijlema, M. An accurate and efficient finite-difference algorithm for non-hydrostatic free-surface flow with application to wave propagation. *Int. J. Numer. Methods Fluids* **2003**, *43*, 1–23. [[CrossRef](#)]
46. Harten, A.; Lax, P.; van Leer, B. On upstream differencing and Godunov-type schemes for hyperbolic conservation laws. *SIAM Rev.* **1983**, *25*, 35–61. [[CrossRef](#)]
47. Toro, E.F.; Spruce, M.; Speares, W. Restoration of the contact surface in the HLL-Riemann solver. *Shock Waves* **1994**, *4*, 25–34. [[CrossRef](#)]
48. Pacanowski, R.C.; Philander, S.G.H. Parameterization of vertical mixing in numerical models of tropical oceans. *J. Phys. Oceanogr.* **1981**, *11*, 1443–1451. [[CrossRef](#)]
49. Large, W.G.; McWilliams, J.C.; Doney, S.C. Oceanic vertical mixing: A review and a model with a nonlocal boundary layer parameterization. *Rev. Geophys.* **1994**, *32*, 363–403. [[CrossRef](#)]

50. Corcos, G.M.; Sherman, F.S. Vorticity concentration and the dynamics of unstable free shear layers. *J. Fluid Mech.* **1976**, *73*, 241–264. [[CrossRef](#)]
51. Winters, K.B.; Lombard, P.N.; Riley, J.J.; D’Asaro, E.A. Available potential energy and mixing in density-stratified fluids. *J. Fluid Mech.* **1995**, *289*, 115–128. [[CrossRef](#)]
52. Dossmann, Y.; Rosevear, M.G.; Griffiths, R.W.; McC. Hogg, A.; Hughes, G.O.; Copeland, M. Experiments with mixing in stratified flow over a topographic ridge. *J. Geophys. Res. Oceans* **2016**, *121*, 6961–6977. [[CrossRef](#)]



© 2019 by the authors. Licensee MDPI, Basel, Switzerland. This article is an open access article distributed under the terms and conditions of the Creative Commons Attribution (CC BY) license (<http://creativecommons.org/licenses/by/4.0/>).